Computers in Biology and Medicine 191 (2025) 110158

Contents lists available at ScienceDirect

Computers in Biology and Medicine

journal homepage: www.elsevier.com/locate/compbiomed

Generation of personalized synthetic 3-dimensional inlet velocity profiles for computational fluid dynamics simulations of type B aortic dissection

Kaihong Wang [a], Chlöe H. Armour [a,b], Lydia Hanna [c,d], Richard Gibbs [c,d], Xiao Yun Xu [a,*]

[a] Department of Chemical Engineering, Imperial College London, London, UK
[b] National Heart and Lung Institute, Imperial College London, London, UK
[c] Department of Surgery and Cancer, Imperial College London, London, UK
[d] Imperial Vascular Unit, Imperial College Healthcare NHS Trust, London, UK

ARTICLE INFO

Keywords:
4D-flow magnetic resonance imaging
Computational fluid dynamics
Statistical shape modelling
3D inlet velocity profile
Wall shear stress
Pressure
Flow distribution

ABSTRACT

Background: Computational fluid dynamics (CFD) simulations have shown promise in assessing type B aortic dissection (TBAD) to predict disease progression, and inlet velocity profiles (IVPs) are essential for such simulations. To truly capture patient-specific hemodynamic features, 3D IVPs extracted from 4D-flow magnetic resonance imaging (4D MRI) should be used, but 4D MRI is not commonly available.

Method: A new workflow was devised to generate personalized synthetic 3D IVPs that can replace 4D MRI-derived IVPs in CFD simulations. Based on 3D IVPs extracted from 4D MRI of 33 TBAD patients, statistical shape modelling and principal component analysis were performed to generate 270 synthetic 3D IVPs accounting for specific flow features. The synthetic 3D IVPs were then scaled and fine-tuned to match patient-specific stroke volume and systole-to-diastole ratio. The performance of personalized synthetic IVPs in CFD simulations was evaluated against patient-specific IVPs and compared with parabolic and flat IVPs.

Results: Our results showed that the synthetic 3D IVP was sufficient for faithful reproduction of hemodynamics throughout the aorta. In the ascending aorta (AAo), where non-patient-specific IVPs failed to replicate *in vivo* flow features in previous studies, the personalized synthetic IVP was able to match not only the flow pattern but also time-averaged wall shear stress (TAWSS), with a mean TAWSS difference of 5.9 %, which was up to 36.5 % by idealized IVPs. Additionally, the predicted retrograde flow index in both the AAo (8.36 %) and descending aorta (8.17 %) matched closely the results obtained with the 4D MRI-derived IVP (7.36 % and 6.55 %). The maximum false lumen pressure difference was reduced to 11.6 % from 68.8 % by the parabolic IVP and 72.6 % by the flat IVP.

Conclusion: This study demonstrates the superiority of personalized synthetic 3D IVPs over commonly adopted parabolic or flat IVPs and offers a viable alternative to 4D MRI-derived IVP for CFD simulations of TBAD.

1. Introduction

Type B aortic dissection (TBAD) is a life-threatening disease of the aorta in which the inner wall of the descending aorta (DAo) is torn, resulting in the separation of the wall layers through which blood persistently flows. This leads to the formation of a false lumen (FL), which may further expand and even rupture [1]. Assessment of FL progression plays an important role in risk stratification and treatment planning. Computational fluid dynamics (CFD) simulations have been adopted extensively to predict aortic hemodynamics such as wall shear stress (WSS) distribution and flow patterns in patient-specific geometries. Abnormal hemodynamics have been found to correlate with disease progressions. In this context, regions characterized by low WSS and high flow stagnancy were indicated as a sign of FL thrombosis [2–5], whilst more retrograde flows through the primary entry tear (PET) were observed in expanding FLs than stable FLs (43.8 % vs. 10.3 %, as quantified by retrograde flow fraction) through 4-dimensional flow magnetic resonance imaging (4D MRI) [6]. Detailed hemodynamic assessments have allowed for predictions of FL development, such as shear-driven thrombosis models [7–10] which can predict the location and extent of FL thrombosis in TBAD.

In patient-specific CFD simulations of aortic flow, physiologically

This article is part of a special issue entitled: Cardiovascular Digital Twins published in Computers in Biology and Medicine.

* Corresponding author. Department of Chemical Engineering, Imperial College London, South Kensington Campus, London SW7 2AZ, UK.
E-mail address: yun.xu@imperial.ac.uk (X.Y. Xu).

https://doi.org/10.1016/j.compbiomed.2025.110158
Received 13 December 2024; Received in revised form 22 March 2025; Accepted 4 April 2025
Available online 10 April 2025

realistic boundary conditions are essential for faithful reproduction of flow features and WSS. The importance of appropriate inlet BCs has been demonstrated in several studies. For example, 3-dimensional inlet velocity profiles (3D IVPs) derived from 4D MRI (as opposed to idealized flat profiles) are desired to accurately capture the spatial variations of velocity especially in aneurysmal or dissected aortas [11–20], and a lack of 3D spatial distribution can lead to significant differences in WSS distributions [16,19,21]. Bozzi et al. [22] also demonstrated that uncertainties in MRI-derived IVP can lead to non-negligible impacts on both flow patterns and WSS distributions. Armour et al. [16] found that a flat IVP resulted in 35 % and 27 % differences in WSS in the PET region and the descending aorta (DAo), respectively. More significant differences were observed in the ascending aorta (AAo) [15]. Similarly, the study of Pirola et al. [17] highlighted the importance of 3D IVPs in simulating flow in the aorta with a diseased aortic valve where significant secondary flows occur. Furthermore, Youssefi et al. [20] investigated the plausibility of flat and parabolic IVPs in replicating flow patterns in the healthy and dilated AAo against the through-plane IVP. Both idealized IVPs resulted in significant alterations in flow patterns in the DAo, especially in replicating highly asymmetric flow distributions.

The shape of inlet flow waveform, characterised by its amplitude and the systole to diastole ratio (SDR), dictates the stroke volume (SV) which also has a strong influence on CFD simulation results. Several sensitivity studies have been carried out, demonstrating significant variability in results due to the shape of inlet flow waveform [23,24]. In addition, it was shown that increasing SV by 25 % resulted in a 11 % increase in WSS in the DAo [19], and this difference could be up to 35 % when reducing SV by 25 % [15]. Furthermore, a recent study by Wang et al. [25] demonstrated that SDR-matched inlet flow waveforms could significantly improve the simulation results even with a flat IVP. Specifically, the difference in time-averaged WSS (TAWSS) was reduced from 54.1 % (with a generic waveform tuned to match SV only) to 5.7 % (with matching SV and SDR) at the PET, and more accurate retrograde flows were captured through the PET. However, there were still considerable discrepancies in the AAo due to the lack of 3D IVPs, since flow jet and secondary flows are prominent features there.

While patient-specific 3D IVPs are only obtainable through 4D MRI, the application of statistical shape models (SSMs) and principal component analysis (PCA) allows for the analysis of flow characteristics and the generation of synthetic profiles that can represent a variety of flow features. This has been demonstrated by Saitta et al. [26] who proposed a workflow to analyze inlet flow features in ascending aortic aneurysms and generated over 300 synthetic 3D IVPs based on a clinical dataset of 33 patients. However, the use of such synthetic IVPs to replace patient-specific IVPs in CFD simulations has not been evaluated. Inspired by their work, the present study aims to develop a workflow to personalize synthetic 3D IVPs based on limited available patient data for faithful reproduction of flow and wall shear stress in both the AAo and DAo. First, SSM and PCA are applied to analyze flow features from 4D MRI of 33 TBAD patients and then to generate a large set of synthetic 3D IVPs. Next, a new workflow is proposed to personalize these synthetic 3D IVPs based on patient-specific SV and SDR which are more easily accessible than 4D MRI. Finally, CFD simulations are performed using patient-specific 3D, synthetic 3D, parabolic, and flat IVPs, for detailed comparisons to evaluate the performance of the proposed method.

2. Method

2.1. Data collection and generation of synthetic inlet velocity profiles

Thirty-three TBAD patients from St Mary's Hospital, London, United Kingdom, with 4D MRI scans acquired between 2021 and 2022 were included for PCA and SSM analysis. One patient was selected for CFD simulations to evaluate the performance of the proposed method. The study was approved by the East of England - Cambridgeshire and Hertfordshire Research Ethics Committee (21/EE/0086, IRAS 294766).

Based on the workflow developed by Saitta et al. [26], 300 synthetic 3D IVPs were generated by adding shape variations to the mean velocity profile. Details of SSM and PCA can be found in the Supplementary Materials, and the workflow is summarized in Fig. S1. In addition, five flow descriptors, peak positive velocity (PPV), flow dispersion index (FDI), flow jet angle (FJA), secondary flow degree (SFD), and retrograde flow index (RFI), were adopted to quantify the statistical difference between the 4D MRI and synthetic dataset. FDI is computed as the area ratio of the region presenting the top 15 % of peak velocity and the inlet area (Equation (1)). FJA is used to quantify the skewness of the inlet flow towards the aortic wall, represented by the angle between the mean velocity direction and the unit vector orthogonal to the inlet surface $\boldsymbol{n}$ (Equation (2)). SFD is defined as the ratio of the mean radial velocity magnitude $\boldsymbol{v}_{\parallel}$ to the mean axial velocity magnitude $\boldsymbol{v}_{\perp}$ (Equation (3)). RFI is calculated as the fraction of retrograde flow rate Q_r relative to the total flow rate (Equation (4)).

$$FDI = \frac{Area^{top15\%}}{Area} * 100\% \tag{1}$$

$$FJA = arcos(\boldsymbol{v}_{mean} \cdot \boldsymbol{n}) \tag{2}$$

$$SFD = \frac{|\boldsymbol{v}_{\parallel}|}{|\boldsymbol{v}_{\perp}|} \tag{3}$$

$$RFI = \frac{\left|\int_0^T Q_r dt\right|}{\left|\int_0^T Q_r dt\right| + \left|\int_0^T Q_a dt\right|} * 100\% \tag{4}$$

where Q_a refers to antegrade flow rate. Acceptance criteria were adopted to avoid unrealistic synthetic IVPs before they were applied to CFD simulations as:

$$I_d = \left[\mu_d - 2\sqrt{\lambda_d}\right] \cup \left[\mu_d + 2\sqrt{\lambda_d}\right] \tag{5}$$

where the interval of acceptance, I_d, is defined based on statistical distributions of the flow descriptors, $\sqrt{\lambda_d}$ is the standard deviation, and μ_d is the mean value of the considered flow descriptors d defined as:

$$\mu_d = \frac{1}{J}\sum_j \frac{1}{T}\sum_t d_t^j \tag{6}$$

If any flow descriptor extracted from the synthetic IVPs fell outside the acceptance intervals, the corresponding IVPs would be filtered out from the next step.

2.2. Personalization of synthetic IVPs

A new workflow was designed to personalize the synthetic 3D IVPs using data available for an individual patient, as illustrated in Fig. 1. First, a generic flow waveform was tuned to match a patient's cardiac period (T), $SV_{patient\text{-}spacific}$, and SDR using the same workflow described in our previous work [25]. One set of synthetic 3D IVP was randomly selected from the synthetic dataset. Then, the flow waveform at the inlet plane was obtained by integrating the normal velocity over the surface area of each inlet element, and the $SV_{synthetic}$ was measured. Temporal alignment was performed to match the timepoint of peak systole to that of the personalized flow waveform generated in the first step. SDR was matched by either extending or truncating the diastole period. Finally, synthetic IVPs were rescaled to match $SV_{patient\text{-}spacific}$ by multiplying each nodal velocity by the $SV_{patient\text{-}spacific}/SV_{synthetic}$ ratio. All IVPs were temporally interpolated to match the patient-specific cardiac period and exported for implementation in ANSYS CFX (Ansys Inc, 2022 R2).

2.3. Computational fluid dynamics simulations

A patient-specific geometry was reconstructed from MRI using semi-

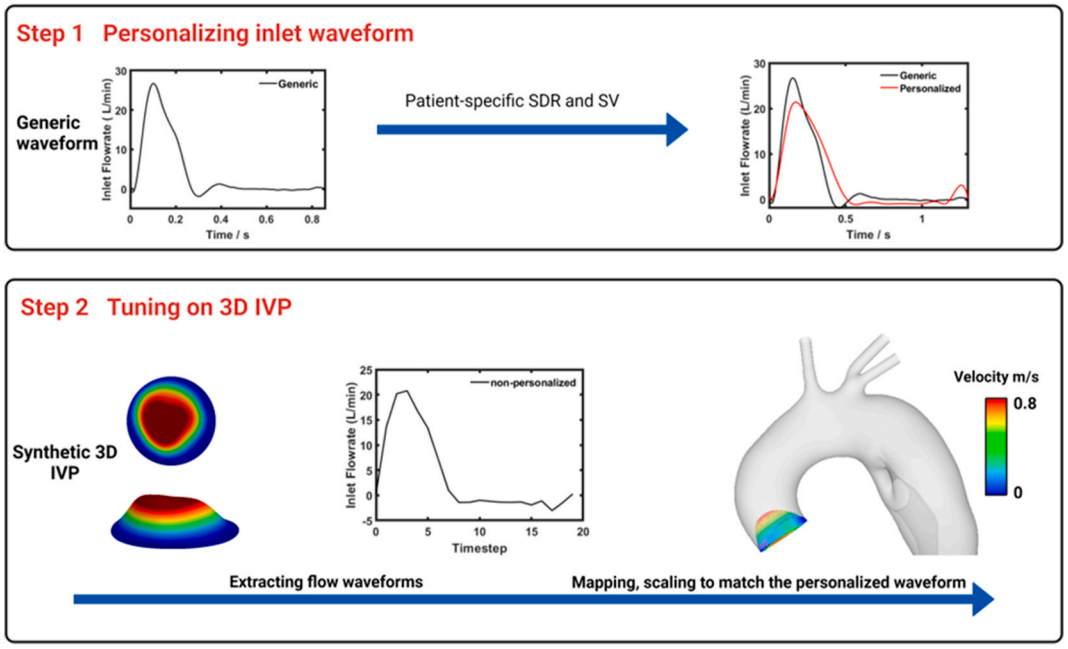

Fig. 1. A workflow for personalizing synthetic 3D IVPs. **Step 1**: Personalizing inlet flow waveforms based on T, SV, and SDR. **Step 2**: Tuning synthetic and parabolic 3D IVPs by aligning the peak systole timepoint, extending or truncating the diastole phase, and scaling SV. **IVP**: inlet velocity profile. **T**: the cardiac period. **SV**: stroke volume. **SDR**: the systole and diastole ratio.

automatic segmentation tools available in Mimics (Materialise HQ, Leuven); these include region growing, mask splitting, and smoothing. Fig. 2 presents the final smoothed geometry that was built for CFD simulations. This geometry was imported into ICEM (Ansys Inc, 2022 R2) and discretized into an unstructured mesh with hexahedral core elements and 10 prism boundary layers. Refinement was applied in regions of tear and small branches. A mesh sensitivity test was conducted to ensure mesh-independent results. Three meshes (coarse, medium, and fine) were generated, with the number of elements approximately doubling for each two neighbouring meshes. Max and mean TAWSS and velocity were compared at four cross-sectional planes throughout the geometry. A final mesh of 4 million elements (medium) was adopted for computational efficiency and accuracy, which showed differences of less than 4 % for all variables at the selected planes compared to the finer mesh. Further quantitative details of the mesh sensitivity analysis can be found in the Supplementary Material.

Table 1
Details of boundary conditions used in 4DMRI, Synthetic 3D, Parabolic and Flat simulations.

Simulation	Inlet boundary condition	Outlet boundary condition
4DMRI	Patient-specific 3D IVPs extracted from 4D-flow MRI	3EWM: tuned based on patient-specific flow and pressure
Synthetic 3D	Personalized synthetic 3D IVP	3EWM: Simplified tuning based on outlet area
Parabolic	Personalized parabolic IVP	3EWM: Simplified tuning based on outlet area
Flat	Flat IVP with personalized flow waveform	3EWM: Simplified tuning based on outlet area

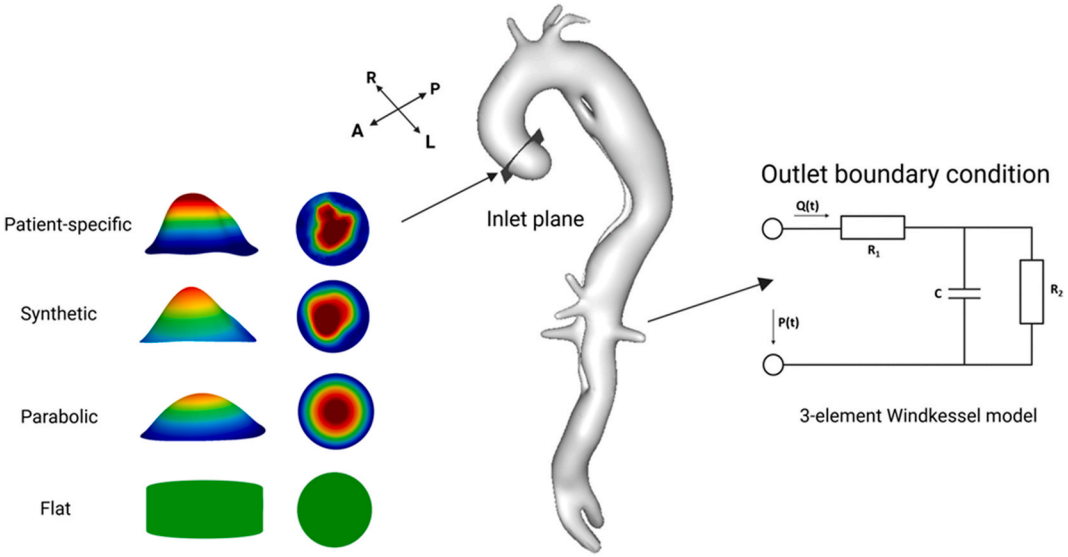

Fig. 2. Reconstructed patient-specific geometry, and boundary conditions used for CFD simulations.

CFD simulations were carried out with 4 different sets of BCs, and details of each set are summarized in Table 1 and Fig. 2. At the inlet, the '4DMRI' simulation implemented the patient-specific 3D IVP extracted from 4D MRI data. For 'Synthetic 3D', a personalized synthetic 3D IVP following the proposed workflow was applied. For 'Parabolic', an idealized parabolic IVP was generated using a circular plane according to Equation (7), where u_{mean} is the mean velocity at the inlet, r is the radial distance, and R_{inlet} is the radius of the inlet plane. The idealized parabolic IVP was personalized using the same workflow shown in Fig. 1. For 'Flat', a flat IVP with personalized inlet flow waveform was applied at the inlet.

$$u(r) = 2u_{mean}\left(1 - \frac{r^2}{R_{inlet}^2}\right) \tag{7}$$

At all outlets, a well-tuned 3-element Windkessel model (3EWM) was applied in the '4DMRI' case, following the tuning procedure presented in the work of Pirola et al [14]. Patient-specific flow split into each branch was measured from 4D MRI, and an aortic pressure of 125/85 mmHg was assumed as a patient-specific pressure measurement was not available [27]. For 'Synthetic 3D', 'Parabolic', and 'Flat', 3EWMs were applied with parameters calculated from a simplified procedure [25] designed to tune parameters when patient-specific MRI is not available (as is assumed in the case of these three simulations). Further details on tuning the 3EWM parameters for each inlet velocity profile can be found in the Supplementary Material.

The flow was assumed to be laminar as the peak Reynolds number of 3706 was below the critical Reynolds number for transition to turbulence according to the study of Kousera et al. [28]. All simulations were run in Ansys CFX (Ansys Inc, 2022 R2) which employs a coupled solver that solves the pressure and velocity equations simultaneously [29,30]. For spatial discretization, a high-resolution advection scheme (combined 1st-order Upwind and 2nd-order central difference) was adopted. A second-order backward Euler scheme was adopted for temporal discretization. The aortic wall was assumed to be rigid with a non-slip condition. Blood was modelled as a non-Newtonian fluid, and the Bird-Carreau model was adopted to account for its shear-thinning behaviour and defined as:

$$\mu = \mu_\infty + (\mu_0 - \mu_\infty)\left[1 + (\lambda\dot{\gamma})^2\right]^{\frac{n-1}{2}} \tag{8}$$

where $\mu_\infty = 0.0035$ Pa s is the high-shear viscosity, $\mu_0 = 0.056$ Pa s is the low-shear viscosity, $\lambda = 3.313$ s is the time constant, and n = 0.3568 is the power law index [31]. Each simulation was run for a total of 5 cardiac cycles with a timestep of 0.001 s. Periodic results were achieved after three cycles, and the last cycle was used for final analysis. Results from 4DMRI were treated as the gold standard for comparison and validation. Qualitative and quantitative assessments were conducted on TAWSS, flow patterns, and pressure in the AAo and DAo. RFI was measured at the AAo and PET. Relative pressure differences between the aortic root and the distal FL were also calculated and normalized by aortic length for comparison.

2.4. Statistical analysis

As the focus of this study was to examine the performance of synthetic 3D IVPs in the AAo, the mean difference in TAWSS compared to the 4DMRI simulation results was calculated for each inlet boundary condition setting. The standard deviation and 95 % limits of agreement were computed to describe the difference. Bland-Altman analysis was performed to assess similarity [32], and Pearson correlation coefficient was also calculated.

3. Results

3.1. Patient-specific and synthetic 3D IVPs

A total of 300 synthetic 3D IVPs were generated, of which 270 passed the acceptance criteria. Fig. 3 shows 15 out of the 270 synthetic 3D IVPs at peak systole, and Fig. 4 presents patient-specific 3D IVPs for 20 out of the 33 patients. For PPV, 4DMRI and synthetic IVPs had a mean value of 0.40 m/s and 0.33 m/s, respectively. For FDI, both 4DMRI and synthetic IVPs exhibited a similar distribution with a mean value of 11.66 % and 13.14 %, respectively. For FJA, 4DMRI and synthetic IVPs had a mean value of 78.15 ° and 76.83 °, respectively. The mean SFDs were 2.50 for 4D MRI IVPs and 2.02 for synthetic IVPs, and the mean RFIs were 7.77 % and 7.81 %, respectively.

Table 2 summarizes the corresponding values of each flow descriptor at peak systole for each boundary condition set. All IVPs showed a similar peak flow rate ranging from 20.38 L/min by the 4DMRI IVP to 22.86 L/min by the parabolic IVP. For flow dispersion index, the 4DMRI IVP presented a value of 16.38 %, and the synthetic and parabolic IVPs had a value of 24.96 % and 24.95 %, respectively. Both the 4DMRI and synthetic IVPs presented a low secondary flow degree with a value of 0.02 and 0.12, respectively.

3.2. Flow patterns

Fig. 5 shows flow distributions on the inlet plane, plane 1 (in the AAo), and plane 2 (at PET) during cardiac systole. On the inlet plane, the synthetic IVP presented a very similar flow distribution to the 4DMRI IVP, which presents high velocities at the centre resembling the shape of the aortic valve during its opening phase, while all other simulations failed to reproduce such flow features. On plane 1, the synthetic IVP captured the location of high velocity flows over the entire systolic phase. The parabolic and flat simulations successfully predicted the location of high velocity flows at peak systole, while they underestimated the flow distributions at other timepoints. On plane 2, all simulations captured a similar flow distribution over cardiac systole, except for the parabolic IVP which underestimated the flow at T1.

Flow patterns were further quantified using RFI. As shown in Fig. 6A, on plane 1, the 4DMRI IVP had a value of 7.36 %, and the synthetic, parabolic, and flat IVPs predicted values of 8.36 %, 3.47 %, and 3.37 %, respectively. On plane 2, the 4DMRI IVP showed a value of 6.55 %, with the synthetic, parabolic, and flat profiles predicting values of 8.17 %, 4.06 %, and 3.76 %, respectively.

3.3. Time-averaged wall shear stress

Fig. 7a shows TAWSS distributions over the entire aorta and localised views of the AAo obtained with the 4DMRI, synthetic 3D, parabolic, and flat IVPs, while Fig. 7b presents the absolute difference of TAWSS compared to the 4DMRI simulation. It can be seen that the 4DMRI IVPs produced spatially varying TAWSS distribution in the AAo, with a high TAWSS hotspot on the outer curvature of AAo and an isolated region of relatively low TAWSS close to the aortic root. The synthetic IVP reproduced this pattern very well, but the parabolic IVP failed to capture the high TAWSS hotspot, whilst the flat IVP underestimated the TAWSS throughout the AAo. In the DAo, all simulations predicted comparable results.

Further analysis was made by examining absolute TAWSS differences compared to the 4DMRI IVP results. As shown in Fig. 7b, notable differences were observed in the AAo, with the synthetic IVP showing the least difference and the flat showing the most. The average TAWSS for the AAo, PET, and DAo were measured and are shown in Fig. 6b. Among all simulations, the synthetic 3D IVP produced TAWSS values that were closest to results of the 4DMRI IVP. In the AAo, the synthetic 3D IVP predicted an average value of 0.90 Pa compared to 0.85 Pa by the 4DMRI IVP. Similarly, in the PET and DAo, the synthetic 3D IVP values

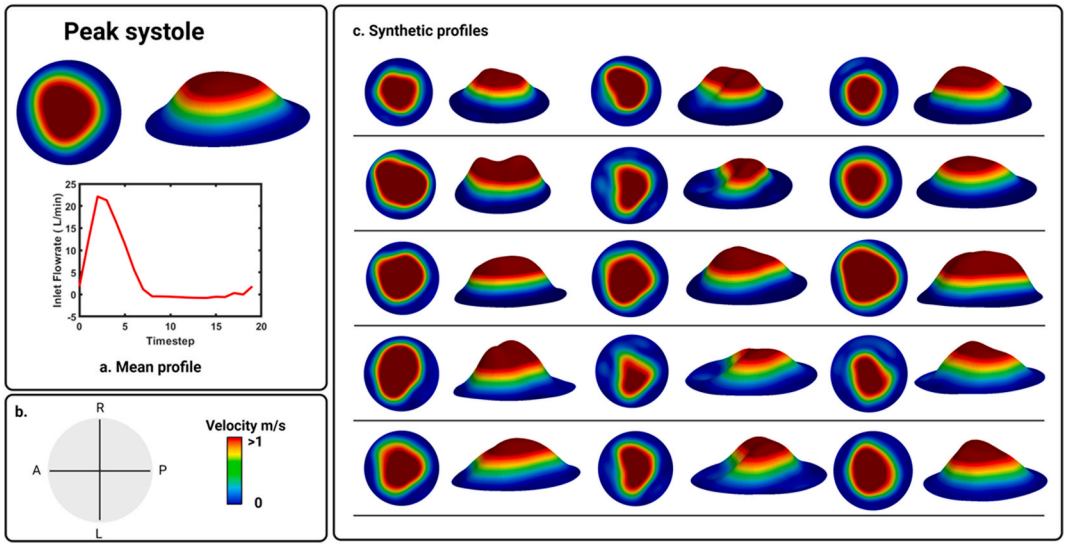

Fig. 3. **a**. Mean synthetic IVP at peak systole and the corresponding inlet flow waveform. **b.** Orientations of the plane and profile. **c.** Distributions of 15 synthetic 3D IVPs at peak systole. **IVP**: inlet velocity profile.

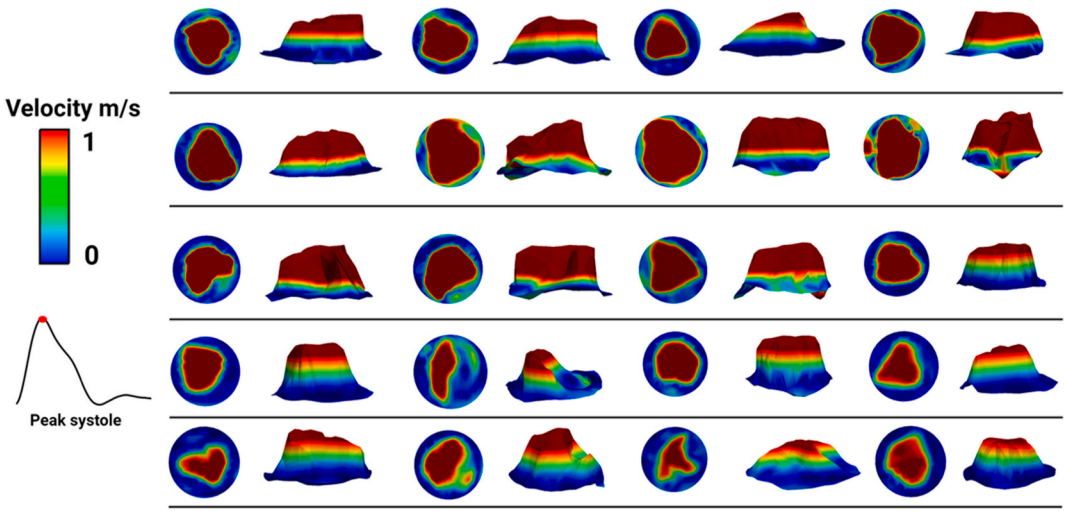

Fig. 4. Patient-specific 3D IVPs for 20 patients. **IVP**: inlet velocity profile.

Table 2
Peak flow rate, flow jet angle, flow dispersion index, secondary flow degree, and retrograde flow fraction on the inlet plane for 4DMRI, synthetic 3D, parabolic, and flat IVPs.

	Peak flow rate (L/min)	Flow jet angle (°)	Flow dispersion index (%)	Secondary flow degree (–)	Retrograde flow index (%)
4DMRI	20.38	1.02	16.38	0.02	7.28
Synthetic 3D	20.84	6.83	24.96	0.12	8.24
Parabolic	22.86	0	24.95	0	3.31
Flat	21.86	0	–	0	3.64

were 0.40 Pa and 0.43 Pa, compared to 0.39 Pa and 0.40 Pa from the 4DMRI IVP, respectively.

Fig. 8 shows Bland-Altman and Pearson correlation plots of mean TAWSS in the AAo by the synthetic IVP, parabolic IVP, and flat IVP against the 4DMRI IVP. As shown in Fig. 8a, over 90 % of points was within the outliers by all IVPs. The synthetic IVP had the least mean difference (red line) of −0.05 Pa with upper and lower limits of 0.24 Pa and −0.34 Pa (green lines), respectively. In Fig. 8b, the strongest positive linear correlation was observed by the synthetic IVP, with a Pearson correlation coefficient of 0.83, while the parabolic IVP showed a weaker linear correlation. No linear correlation was observed by the flat IVP.

3.4. Pressure

Fig. 9a shows aortic pressure difference per unit length ΔP over the cardiac cycle for the simulations with 4DMRI, synthetic, parabolic and flat IVPs. All simulations produced similar variations over the cardiac cycle, with the maximum pressure drop occurring within the first 0.2 s. The 4DMRI and synthetic IVPs showed similar ΔP fluctuations in diastole, which were not captured by the parabolic and flat IVPs. The maximum pressure difference, ΔP_{max}, was measured for each simulation and compared in Fig. 9b. The synthetic 3D IVP produced a maximum pressure difference of 7.53 mmHg/m that was closest to 6.75 mmHg/m by the 4DMRI IVP.

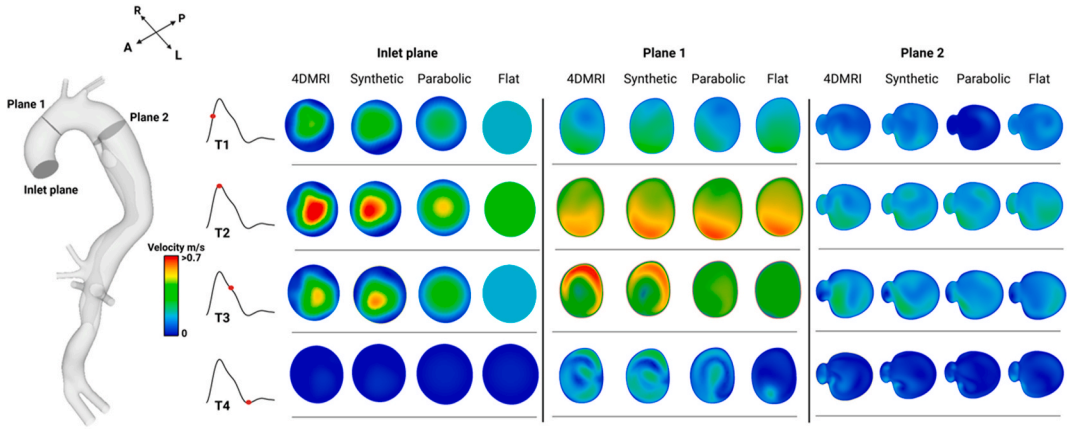

Fig. 5. Flow distributions on the inlet plane, plane 1 and plane 2 at systolic acceleration (T1), peak systole (T2), systolic deceleration (T3), and the end of systole (T4).

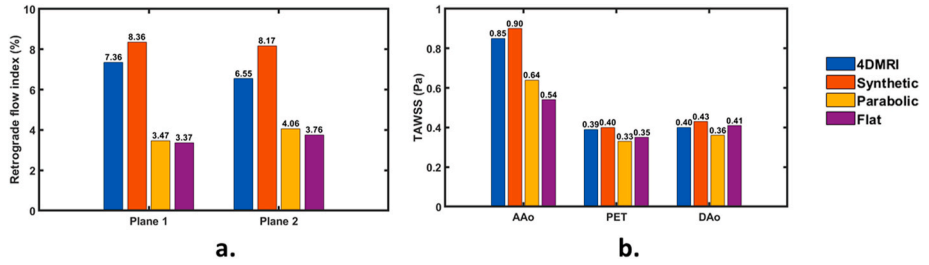

Fig. 6. a. Retrograde flow index on plane 1 and 2 over a cardiac cycle. **b.** Mean TAWSS in the AAo, PET and DAo. **TAWSS**: time-averaged wall shear stress. **AAo**: the ascending aorta. **PET**: the primary entry tear. **DAo**: the descending aorta.

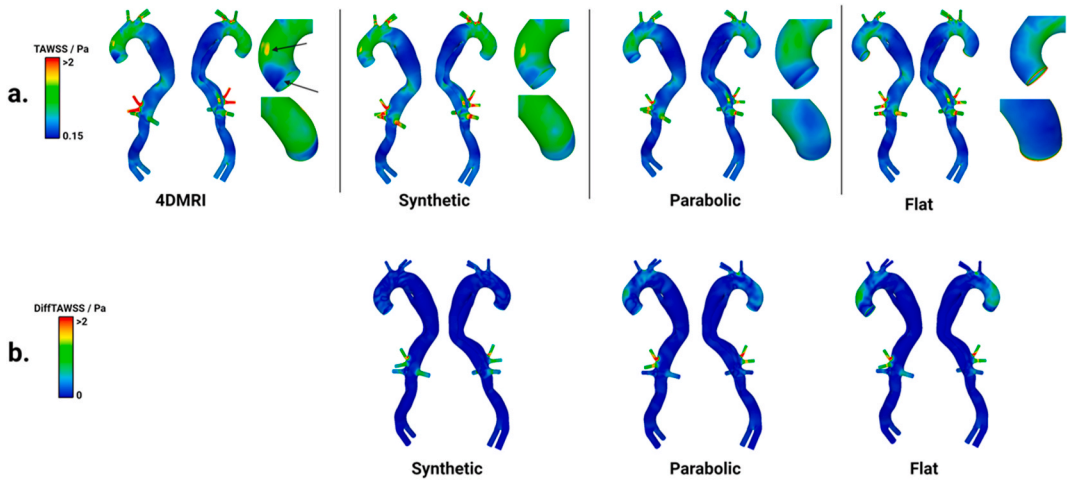

Fig. 7. a. Time-averaged wall shear stress (TAWSS) distributions obtained with the 4DMRI, synthetic, parabolic and flat IVPs. **b.** Absolute difference of TAWSS compared to the 4DMRI simulation results.

4. Discussion

CFD simulations have shown great potential in providing detailed hemodynamic assessments of the aorta which could assist in the diagnosis of cardiovascular diseases and prediction of disease progression. In TBAD, hemodynamics plays an important role in true lumen and FL remodelling. Recent studies have shown that substantial retrograde flow entering the FL through the PET could indicate rapid aortic growth [33,34]. A higher pressure within the FL compared to the aortic root has been identified as an independent risk predictor of FL enlargement [34]. In addition, hemodynamic-based models have been used to predict the location and extent of FL thrombosis as demonstrated in our previous studies [8–10]. Long residence time, low TAWSS, and WSS on the formed thrombus are critical in initiating and regulating the formation, growth and breakdown of thrombus. As a result, both physiologically realistic and personalized boundary conditions should be applied to ensure the reliability of simulation-based assessments.

This study presents, for the first time, a novel workflow to generate and then personalize synthetic 3D IVPs for patient-specific CFD simulations of TBAD. Advancing on the work of Saitta et al. [26], the generated synthetic 3D IVPs were further tuned to match patient-specific cardiac cycle characteristics and stroke volume, which

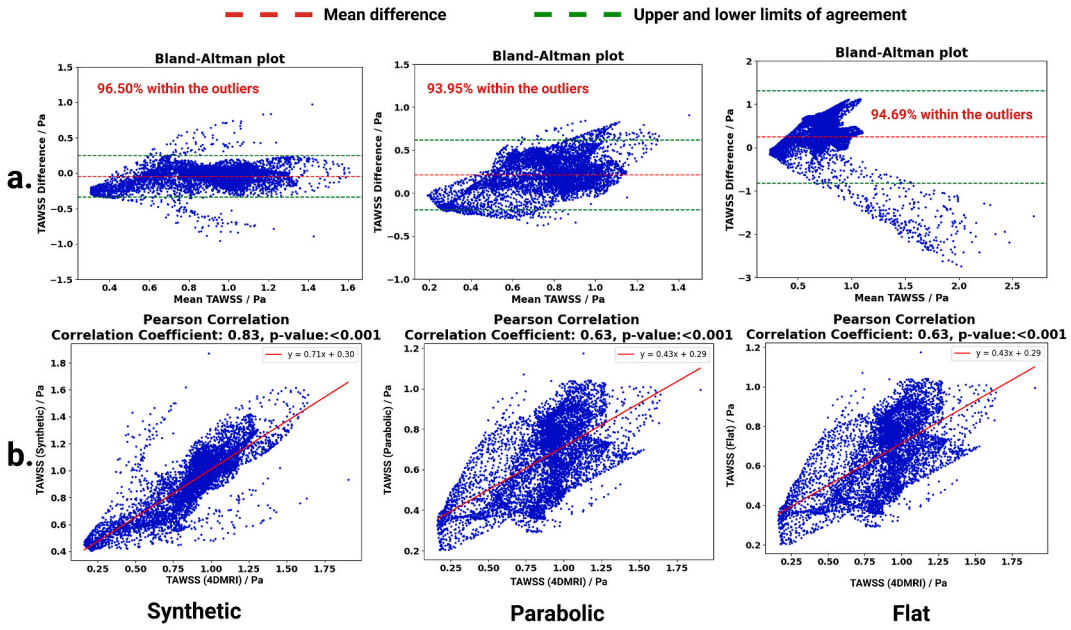

Fig. 8. **a**. Bland-Altman plots of time-averaged wall shear stress (TAWSS) measurements in the ascending aorta (AAo) by the synthetic 3D inlet velocity profile (IVP), the parabolic IVP, and the flat IVP against the 4DMRI IVP. **b**. Pearson correlation of TAWSS between the 4DMRI IVP and the synthetic 3D IVP, the parabolic IVP, and the flat IVP. The best-fit line is shown in red. (For interpretation of the references to colour in this figure legend, the reader is referred to the Web version of this article.)

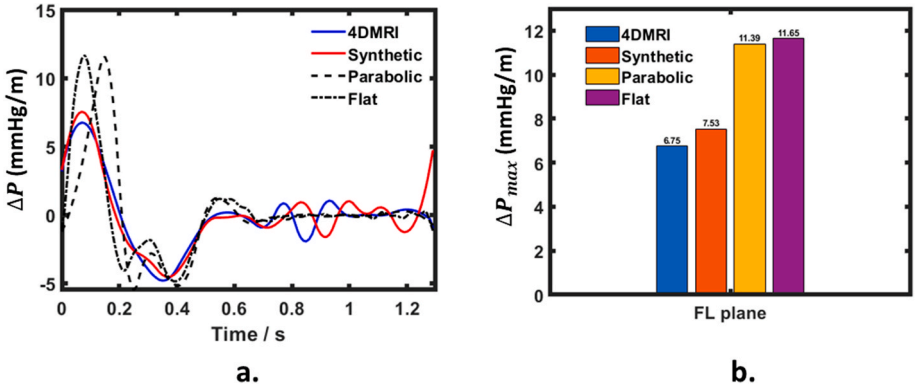

Fig. 9. **a**. Variations of false lumen relative pressure difference over a cardiac cycle by the 4DMRI, synthetic, parabolic and flat IVP simulations. **b.** Maximum pressure difference, ΔP_{max}, measured for each simulation.

have been shown to reduce errors in predicted hemodynamics in the DAo [25]. Simulations were carried out on a representative TBAD patient using 4DMRI, synthetic, parabolic and flat IVPs, and hemodynamic parameters, such as retrograde flow index, WSS and pressure, were compared and validated against the patient-specific 4DMRI simulation.

A total of 270 synthetic 3D IVPs suitable for CFD simulations of TBAD were generated. These synthetic IVPs differed from those for ascending aortic aneurysms [26] in that they had a smaller FJA with a mean angle of 4.15 ° and a lager mean FDI of 13 % at peak systole. This suggests that synthetic 3D IVPs generated for a specific patient cohort (e.g. ascending aortic aneurysm) may not be suitable for CFD simulations of different aortic diseases.

The synthetic 3D IVPs successfully reproduced flow characteristics in the 4DMRI IVPs, including secondary flows and high velocity jets which have been found to significantly affect WSS-related metrics in the AAo [17], whereas both the parabolic and flat IVPs failed to capture such features. Consequently, when measured against simulation results obtained with the 4DMRI IVP, the synthetic IVP produced a 5.9 % difference in TAWSS in the AAo, which was much smaller than 24.8 % by the parabolic IVP and 36.5 % by the flat IVP. On the other hand, hemodynamic metrics in the PET and DAo were less sensitive to the shape of IVP, with maximum differences ranging from 2.6 % to 15.4 % among all simulations. This is consistent with previous studies which demonstrated that the choice of IVPs has less impact in the DAo [15,19]. In addition, comparisons of RFI and maximum relative FL pressure difference also showed that the synthetic 3D IVP delivered the most accurate predictions among all simulations. As the aforementioned hemodynamic parameters are crucial in predicting aortic growth in TBAD, any improvement in the confidence and fidelity of computational assessments would further enhance their value in clinical applications.

Due to the symmetrical nature of IVPs in most cases, except in patients with aortic valve diseases, the parabolic IVP has been recommended as an efficient alternative [20,35–37]. Rather than only focusing on the DAo [35], our study quantitively validated TAWSS and flow distributions across the whole aorta against the 4DMRI IVP. In the representative TBAD case, the parabolic IVP showed the most significant differences in the AAo, failing to replicate flows and high TAWSS regions in the AAo (Figs. 5 and 7). Furthermore, Bland-Altman analysis

confirmed that the synthetic 3D IVP achieved the best agreement in TAWSS distributions in the AAo, and Pearson correlation analysis also indicated a more positive linear correlation by the synthetic IVP than by the parabolic IVP. Although only one case was evaluated in this study, the synthetic IVP had a Pearson correlation efficient of 0.83. Therefore, unless patients present with a diseased or prosthetic valve, the synthetic 3D IVP and proposed personalizing workflow should be recommended as the inlet boundary condition for CFD simulations of TBAD.

A personalized synthetic 3D IVP allowed patient-specific flow features in the AAo to be preserved in CFD simulations of TBAD, which was not possible with commonly used flat or parabolic inlet velocity profiles. From Table 2, while the parabolic IVP had a FDI similar to the synthetic 3D IVP, a lack of jet and secondary flows likely accounted for inaccuracies in the AAo. There were notable differences in FJA and SFD between the 4DMRI and synthetic IVPs, and sensitivity tests on FJA and SFD will be conducted in the future. In addition, although the synthetic 3D IVP was selected following no specific criteria in this study, it would be valuable to investigate different synthetic 3D IVPs. A set of criteria may be necessary for selecting the most appropriate synthetic IVP for a given patient geometry.

A major assumption made in this study was to treat the aortic wall and intimal flap as rigid. It has been shown that their deformation can affect the distribution and magnitude of low WSS [38,39]. The mobility of the intimal flap also impacts the flow distribution into the TL and FL [40] and pressure difference between the TL and FL [40–42]. However, for the purpose of evaluating the new synthetic 3D IVPs in comparison with other IVPs, the rigid wall assumption would not affect the conclusions drawn. In addition, only one case was included in the validation. Future validations will be conducted on a larger cohort to enhance the reliability of the proposed workflow.

5. Conclusion

This study presented, for the first time, an efficient workflow for setting up physiologically accurate boundary conditions for CFD simulations of TBAD, utilizing basic patient-specific information that can be acquired relatively easily. This workflow effectively addressed an important limitation in patient-specific computational studies when 3D IVPs are unavailable, as 4D MRI is not commonly performed due to its high costs and long scanning time. By validating against the 4DMRI IVP, we demonstrated that the personalized synthetic 3D IVP not only reproduced key hemodynamic features in the AAo, but also performed better in the PET and DAo than the parabolic and flat IVP. Our results show clearly that idealized parabolic and flat profiles are insufficient for CFD simulations of the AAo, and that a synthetic 3D IVP preserves the original flow features in the entire aorta. It is recommended that our synthetic 3D IVPs, personalized based on stroke volume and systole to diastole ratio (which can be readily extracted from electrocardiogram), are used in future CFD studies of TBAD. This work greatly enhances the fidelity of computational assessments of TBAD and allows the application of computational modelling to large patient cohorts when patient-specific 4D MRI data are not available.

CRediT authorship contribution statement

Kaihong Wang: Writing – review & editing, Writing – original draft, Visualization, Validation, Software, Methodology, Investigation, Formal analysis. **Chlöe H. Armour:** Writing – review & editing, Validation, Supervision, Software, Methodology, Investigation, Funding acquisition, Formal analysis. **Lydia Hanna:** Writing – review & editing, Investigation, Funding acquisition, Formal analysis, Data curation, Conceptualization. **Richard Gibbs:** Writing – review & editing, Supervision, Resources, Investigation, Funding acquisition, Conceptualization. **Xiao Yun Xu:** Writing – review & editing, Supervision, Resources, Funding acquisition, Formal analysis, Conceptualization.

Data availability

The source code of personalizing the inlet velocity profiles can be found through: https://github.com/kw1218/Personalizing-3DIVP-TBAD.

Ethics statement

The study was approved by the East of England - Cambridgeshire and Hertfordshire Research Ethics Committee (21/EE/0086, IRAS 294766) in May 2022.

Funding

This work was supported in part by the Rosetrees Trust (Seedcorn2020\100066). CHA was supported by Imperial College London British Heart Foundation Centre of Research Excellence (RE/18/4/34215).

Declaration of competing interest

The authors declare that they have no known competing financial interests or personal relationships that could have appeared to influence the work reported in this paper.

Appendix A. Supplementary data

Supplementary data to this article can be found online at https://doi.org/10.1016/j.compbiomed.2025.110158.

References

[1] Z.A. Zilber, A. Boddu, S.C. Malaisrie, A.W. Hoel, C.K. Mehta, P. Vassallo, N. S. Burris, A. Roldan-Alzate, J.D. Collins, C.J. Francois, B.D. Allen, Noninvasive morphologic and hemodynamic evaluation of type B aortic dissection: state of the art and future perspectives, Radiol Cardioth. Imag. 3 (2021) e200456.
[2] Z. Cheng, N.B. Wood, R.G. Gibbs, X.Y. Xu, Geometric and flow features of type B aortic dissection: initial findings and comparison of medically treated and stented cases, Ann. Biomed. Eng. 43 (2015) 177–189.
[3] V. Butty, K. Gudjonsson, P. Buchel, V. Makhijani, Y. Ventikos, D. Poulikakos, Residence times and basins of attraction for a realistic right internal carotid artery with two aneurysms, Biorheology 39 (2002) 387–393.
[4] X. Jiang, D. Li, P. Wu, X. Li, T. Zheng, A two-fluid blood stasis model for false lumen thrombosis after type B dissection repair, Comput. Methods Biomech. Biomed. Eng. 25 (2022) 1499–1508.
[5] V. Rayz, L. Boussel, L. Ge, J. Leach, A. Martin, M. Lawton, C. Mcculloch, D. Saloner, Flow residence time and regions of intraluminal thrombus deposition in intracranial aneurysms, Ann. Biomed. Eng. 38 (2010) 3058–3069.
[6] N.S. Burris, D.A. Nordsletten, J.A. Sotelo, R. Grogan-Kaylor, I.B. Houben, C. A. Figueroa, S. Uribe, H.J. Patel, False lumen ejection fraction predicts growth in type B aortic dissection: preliminary results, Eur. J. Cardio. Thorac. Surg. 57 (2020) 896–903.
[7] C. Menichini, Z. Cheng, R.G. Gibbs, X.Y. Xu, Predicting false lumen thrombosis in patient-specific models of aortic dissection, J. R. Soc. Interface 13 (2016) 20160759.
[8] C. Menichini, Z. Cheng, R.G. Gibbs, X.Y. Xu, A computational model for false lumen thrombosis in type B aortic dissection following thoracic endovascular repair, J. Biomech. 66 (2018) 36–43.
[9] C.H. Armour, C. Menichini, L. Hanna, R.G. Gibbs, X.Y. Xu, Computational Modeling of Flow and Thrombus Formation in Type B Aortic Dissection: the Influence of False Lumen Perfused Side Branches. *Solid (Bio) Mechanics: Challenges Of the Next Decade*, Springer, 2022.
[10] K. Wang, C.H. Armour, R.G. Gibbs, X.Y. Xu, A numerical study of the effect of thrombus breakdown on predicted thrombus formation and growth, Biomech. Model. Mechanobiol. 23 (2024) 61–71.
[11] F. Tajeddini, D.A. Romero, D. Mcclarty, J. Chung, C. Amon, Workflow comparison for combined 4D MRI/CFD patient-specific cardiovascular flow simulations of the thoracic aorta, J. Fluid Eng. 145 (2023) 061106.
[12] C. Stokes, F. Haupt, D. Becker, V. Muthurangu, H. VON Tengg-Kobligk, S. Balabani, V. Díaz-Zuccarini, The Influence of Minor Aortic Branches in Type-B Aortic Dissection: Patient-specific Flow Simulations Informed by 4D-Flow MRI, 2022.
[13] C. Stokes, M. Bonfanti, Z. Li, J. Xiong, D. Chen, S. Balabani, V. Díaz-Zuccarini, A novel MRI-based data fusion methodology for efficient, personalised, compliant simulations of aortic haemodynamics, J. Biomech. 129 (2021) 110793.

[14] S. Pirola, B. Guo, C. Menichini, S. Saitta, W. Fu, Z. Dong, X.Y. Xu, 4-D flow MRI-based computational analysis of blood flow in patient-specific aortic dissection, IEEE (Inst. Electr. Electron. Eng.) Trans. Biomed. Eng. 66 (2019) 3411–3419.
[15] C.H. Armour, B. Guo, S. Pirola, S. Saitta, Y. Liu, Z. Dong, X.Y. Xu, The influence of inlet velocity profile on predicted flow in type B aortic dissection, Biomech. Model. Mechanobiol. 20 (2021) 481–490.
[16] C.H. Armour, B. Guo, S. Saitta, S. Pirola, Y. Liu, Z. Dong, X.Y. Xu, Evaluation and verification of patient-specific modelling of type B aortic dissection, Comput. Biol. Med. (2021) 105053.
[17] S. Pirola, O. Jarral, D. O'Regan, G. Asimakopoulos, J. Anderson, J. Pepper, T. Athanasiou, X. Xu, Computational study of aortic hemodynamics for patients with an abnormal aortic valve: the importance of secondary flow at the ascending aorta inlet, APL Bioeng. 2 (2018) 026101.
[18] A. Mariotti, S. Celi, M.N. Antonuccio, M.V. Salvetti, Impact of the spatial velocity inlet distribution on the hemodynamics of the thoracic aorta, Cardiova. Eng. Technol. 14 (2023) 713–725.
[19] C. Stokes, D. Ahmed, N. Lind, F. Haupt, D. Becker, J. Hamilton, V. Muthurangu, H. VON Tengg-Kobligk, G. Papadakis, S. Balabani, Aneurysmal growth in type-B aortic dissection: assessing the impact of patient-specific inlet conditions on key haemodynamic indices, J. R. Soc. Interface 20 (2023) 20230281.
[20] P. Youssefi, A. Gomez, C. Arthurs, R. Sharma, M. Jahangiri, C. Alberto Figueroa, Impact of patient-specific inflow velocity profile on hemodynamics of the thoracic aorta, J. Biomech. Eng. 140 (2018) 011002.
[21] U. Morbiducci, R. Ponzini, D. Gallo, C. Bignardi, G. Rizzo, Inflow boundary conditions for image-based computational hemodynamics: impact of idealized versus measured velocity profiles in the human aorta, J. Biomech. 46 (2013) 102–109.
[22] S. Bozzi, U. Morbiducci, D. Gallo, R. Ponzini, G. Rizzo, C. Bignardi, G. Passoni, Uncertainty propagation of phase contrast-MRI derived inlet boundary conditions in computational hemodynamics models of thoracic aorta, Comput. Methods Biomech. Biomed. Eng. 20 (2017) 1104–1112.
[23] A. Mariotti, A. Boccadifuoco, S. Celi, M. Salvetti, Hemodynamics and stresses in numerical simulations of the thoracic aorta: stochastic sensitivity analysis to inlet flow-rate waveform, Comput. Fluid 230 (2021) 105123.
[24] D. Gallo, G. DE Santis, F. Negri, D. Tresoldi, R. Ponzini, D. Massai, M.A. Deriu, P. Segers, B. Verhegghe, G. Rizzo, On the use of in vivo measured flow rates as boundary conditions for image-based hemodynamic models of the human aorta: implications for indicators of abnormal flow, Ann. Biomed. Eng. 40 (2012) 729–741.
[25] K. Wang, C.H. Armour, B. Guo, Z. Dong, X.Y. Xu, A new method for scaling inlet flow waveform in hemodynamic analysis of aortic dissection, Intern. J. Nume. Methods in Biomed. Eng. (2024) e3855.
[26] S. Saitta, L. Maga, C. Armour, E. Votta, D.P. O'Regan, M.Y. Salmasi, T. Athanasiou, J.W. Weinsaft, X.Y. Xu, S. Pirola, Data-driven generation of 4D velocity profiles in the aneurysmal ascending aorta, Comput. Methods Progr. Biomed. 233 (2023) 107468.
[27] L. Morris, P. Tierney, N. Hynes, S. Sultan, An in vitro assessment of the haemodynamic features occurring within the true and false lumens separated by a dissection flap for a patient-specific type B aortic dissection, Front. Cardiovasc. Med. 9 (2022).
[28] C. Kousera, N. Wood, W. Seed, R. Torii, D. O'Regan, X. Xu, A numerical study of aortic flow stability and comparison with in vivo flow measurements, J. Biomech. Eng. 135 (2013) 011003.
[29] C.M. Rhie, W.-L. Chow, Numerical study of the turbulent flow past an airfoil with trailing edge separation, AIAA J. 21 (1983) 1525–1532.
[30] S. Patankar, Numerical Heat Transfer and Fluid Flow, CRC press, 2018.
[31] Y.I. Cho, K.R. Kensey, Effects of the non-Newtonian viscosity of blood on flows in a diseased arterial vessel. Part 1: steady flows, Biorheology 28 (1991) 241–262.
[32] J.M. Bland, D.G. Altman, Agreement between methods of measurement with multiple observations per individual, J. Biopharm. Stat. 17 (2007) 571–582.
[33] A. Evangelista, V. Pineda, A. Guala, B. Bijnens, H. Cuellar, P. Rudenick, A. Sao-Aviles, A. Ruiz, G. Teixido-Tura, R. Rodriguez-Lecoq, False lumen flow assessment by magnetic resonance imaging and long-term outcomes in uncomplicated aortic dissection, J. Am. Coll. Cardiol. 79 (2022) 2415–2427.
[34] D. Marlevi, J.A. Sotelo, R. Grogan-Kaylor, Y. Ahmed, S. Uribe, H.J. Patel, E. R. Edelman, D.A. Nordsletten, N.S. Burris, False lumen pressure estimation in type B aortic dissection using 4D flow cardiovascular magnetic resonance: comparisons with aortic growth, J. Cardiovasc. Magn. Reson. 23 (2021) 51.
[35] Z. Li, S. Liang, H. Xu, M. Zhu, Y. Mei, J. Xiong, D. Chen, Flow analysis of aortic dissection: comparison of inflow boundary conditions for computational models based on 4D PCMRI and Doppler ultrasound, Comput. Methods Biomech. Biomed. Eng. 24 (2021) 1251–1262.
[36] I.C. Campbell, J. Ries, S.S. Dhawan, A.A. Quyyumi, W.R. Taylor, J.N. Oshinski, Effect of Inlet Velocity Profiles on Patient-specific Computational Fluid Dynamics Simulations of the Carotid Bifurcation, 2012.
[37] Y. Qiao, L. Mao, Y. Wang, J. Luan, Y. Chen, T. Zhu, K. Luo, J. Fan, Hemodynamic effects of stent-graft introducer sheath during thoracic endovascular aortic repair, Biomech. Model. Mechanobiol. 21 (2022) 419–431.
[38] M.Y. Chong, B. Gu, B.T. Chan, Z.C. Ong, X.Y. Xu, E. Lim, Effect of intimal flap motion on flow in acute type B aortic dissection by using fluid-structure interaction, Intern. J. Nume. Methods in Biomed. Eng. 36 (2020) e3399.
[39] Y. Qiao, Y. Zeng, Y. Ding, J. Fan, K. Luo, T. Zhu, Numerical simulation of two-phase non-Newtonian blood flow with fluid-structure interaction in aortic dissection, Comput. Methods Biomech. Biomed. Eng. 22 (2019) 620–630.
[40] K. Bäumler, V. Vedula, A.M. Sailer, J. Seo, P. Chiu, G. Mistelbauer, F.P. Chan, M. P. Fischbein, A.L. Marsden, D. Fleischmann, Fluid–structure interaction simulations of patient-specific aortic dissection, Biomech. Model. Mechanobiol. 19 (2020) 1607–1628.
[41] M. Bonfanti, S. Balabani, J.P. Greenwood, S. Puppala, S. Homer-Vanniasinkam, V. Díaz-Zuccarini, Computational tools for clinical support: a multi-scale compliant model for haemodynamic simulations in an aortic dissection based on multi-modal imaging data, J. R. Soc. Interface 14 (2017) 20170632.
[42] K. Bäumler, M. Rolf-Pissarczyk, R. Schussnig, T.-P. Fries, G. Mistelbauer, M. R. Pfaller, A.L. Marsden, D. Fleischmann, G.A. Holzapfel, Assessment of aortic dissection remodeling with patient-specific fluid-structure interaction models, IEEE (Inst. Electr. Electron. Eng.) Trans. Biomed. Eng. 72 (3) (2025) 953–964.